Damping Controller Integrated into Output Current Control Loop and Design for Multiple Servo Drive Systems Connected to Common DC-Bus Line

Katsuki Miura
Dept. of Electrical, Electronics, and Information Engineering
Nagaoka University of Technology
Niigata, Japan
k_miura@stn.nagaokaut.ac.jp

Hiroki Watanabe
Dept. of Electrical, Electronics, and Information Engineering
Nagaoka University of Technology
Niigata, Japan
hwatanabe@vos.nagaokaut.ac.jp

Jun-ichi Itoh
Dept. of Electrical, Electronics, and Information Engineering
Nagaoka University of Technology
Niigata, Japan
itoh@vos.nagaokaut.ac.jp

Takeshi Kiribuchi
OMRON Corporation
Kyoto, Japan
takeshi.kiribuchi@omron.com

Hiroyuki Tokusaki
OMRON Corporation
Kyoto, Japan
hiroyuki.tokusaki@omron.com

Abstract— **This paper proposes a damping control to stabilize multiple servo drive systems connected to a common DC-bus line. The DC-bus servo drive system has a system instability problem due to interference between a constant power load and bus impedance. The damping controller integrated into the output current control loop evaluates the influence of the damping controller on the current response compared with the second-order standard form. The parameters of the damping controller for the multiple units are designed by the impedance method. The experimental results mention that the output current response almost agrees with that of the simulation within a 1% error. Furthermore, the stable operation range with the proposed damping control is expanded by 28% of the motor-rated power.**

Keywords— DC-Bus System, Servo Drive, Damping Control, Impedance-based Stability Analysis

I. Introduction

In recent years, servo drive systems have been used widely in industrial applications. It is generally required to achieve high control performance, low noise, and high power density[1-5]. The control panel, including servo drivers and servo motors, are connected to three-phase AC lines in the conventional configuration of the servo drive systems. However, the conventional configuration has a problem, which is a radiated noise from the AC lines due to the inverter switching. Thus, the countermeasure for the radiation noise is needed in order to prevent interference from other equipment. However, the countermeasure, shielding cables, and layout of power and signal lines lead to increase costs.

In order to solve this problem, the DC-bus servo drive system, which connects the servo drivers to a common DC-bus line, has been proposed [6]. This configuration reduces the radiated noise due to the shorter length of the AC power line and the system loss due to no rectifier stage in each servo driver. Moreover, the DC-bus servo drive systems prevent complicated wiring and reduce the costs of noise suppression since the number of long power lines is reduced.

However, the DC-bus servo drive systems have the problem of system instability due to the interference between the line impedance of the DC-bus and the negative impedance characteristics of the constant power load [7-8]. This problem leads to a system trip due to oscillation in the bus current and voltage when the system is unstable. Therefore, damping control is needed for the DC-bus servo drive system in order to prevent system instability. The damping control method for the DC-bus system and cascaded DC-DC converter have been proposed [9-15]. In these papers, the parameters of the damping controllers are designed based on the impedance method, which analysis the system stability from each subsystem impedance [16]. The impedance method is suitable for the system analysis method for multiple units systems. However, the damping controller influences the output current control performance, such as significant overshoot, due to zeros in the damping controller.

Ref. [17] has proposed the damping controller integrated into the output current controller for a matrix converter. This damping control method evaluates the influence of the damping controller quantitatively from the closed-loop transfer function of the output current controller by comparison with the second-order standard form. Thus, this method is suitable for the DC-bus servo drive system, which is required high torque control accuracy. However, the parameter design method in Ref. [17], that by the linear model of the whole system, has a problem with the extensibility of multiple units system because the linear model is complex due to interference among each unit.

This paper proposes a damping controller integrated into the q-axis current control loop and parameters design method for the multiple DC-bus servo drive systems. The proposed damping controller is inserted into the feedback path of the q-axis current control loop. The current control performance is evaluated by comparison with the standard second-order form. In addition, the proposed parameter design method is based on the impedance method, which analyzes the system stability from the impedance of each subsystem. The originality of this paper is that the damping controller parameters are designed based on the impedance method expanded the multiple units system.

The paper is organized as follows: firstly, the DC-bus servo drive system and its damping controller are described. Secondly, the system stability is analyzed by the impedance method. Thirdly, the proposed design flow for the damping parameters is described. Finally, the proposed design method

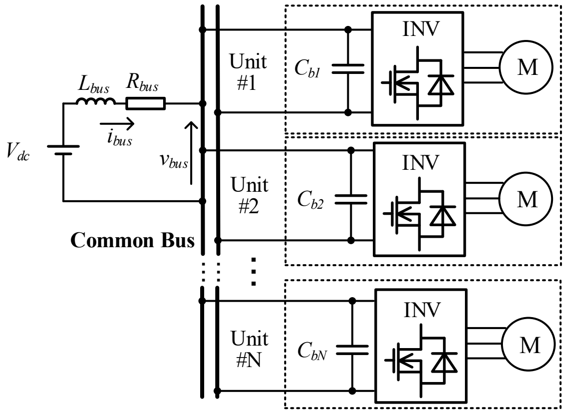

Fig. 1. The DC-bus servo drive system. Each servo unit is connected to a common DC-bus line. The DC-bus line has a large impedance due to its long length.

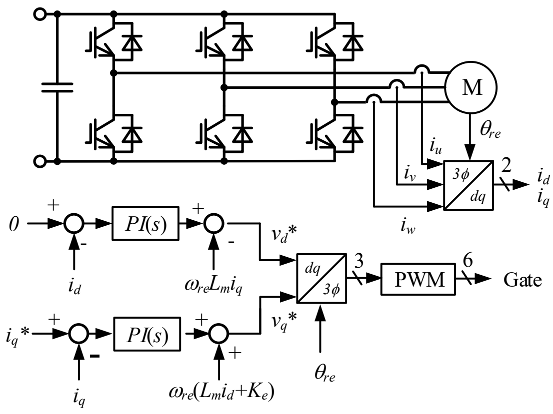

Fig. 2. The configuration of each servo driver. The controller of each unit is based on Field Oriented Control (FOC). Zero-d-axis-current control and decoupling control are also applied.

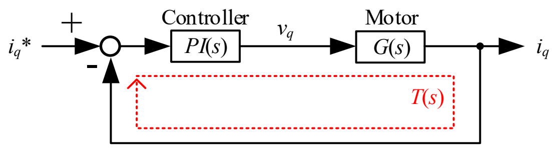

Fig. 3. The simplified control block diagram of each servo unit without the damping controller. The zero-d-axis-current(i_d=0) control and the decoupling control are implemented for the PM motor.

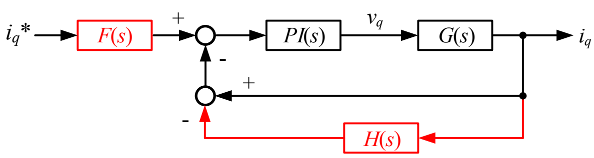

Fig. 4. The control block diagram with the damping controller integrated into the output current control loop. The first-order delay $F(s)$ is inserted into the current command in order to cancel the zeros of the damping controller.

is evaluated by the experiment and discussed in terms of the impact of the influence of the controller delay.

II. System Configuration of DC-Bus Servo Drive System

A. System configuration

Fig. 1 shows the system configuration of the DC-bus servo drive system. Each unit is connected to a common DC-bus line. In this system, the servo driver is placed near the motor. In Fig. 1, L_{bus} is the bus inductance, R_{bus} is the bus resistance, and C_{bk} (k = 1, 2, ... N) is the DC-link capacitor of each servo driver. Note that the DC-bus line has a large impedance due to its long length. In this paper, the system with two servo units is analyzed.

B. Controller configuration of each servo driver

Fig. 2 shows the main circuit and controller configuration of each servo unit without the damping controller. The output current controller is based on Field Oriented Control (FOC) for the servo motor. In Fig. 2, θ_{re} is the rotor position detected by the encoder, $PI(s)$ is the Proportional-Integration regulator for the output current control, ω_{re} is the rotor angular speed, L_m is the inductance of the motor, and K_e is the back-EMF constant of the motor. Zero-d-axis-current(i_d=0) control and decoupling control for canceling cross term of permanent magnet(PM) motor. The gate pulses for each output voltage of the inverter are generated by pulse width modulation(PWM).

The transfer function of the PI controller for current control is expressed as

$$PI(s) = K_p\left(1+\frac{1}{sT_i}\right) \quad (1),$$

where K_p is the proportional gain, and T_i is the integral time. The parameters of the PI controller are designed to cancel zeros as

$$\begin{cases} K_p = \omega_c L_m \\ T_i = L_m / R_a \end{cases} \quad (2),$$

where R_a is the armature resistance, and ω_c is the bandwidth of the current controller.

Fig. 3 shows the simplified q-axis control block diagram under id=0 control of each servo driver without the damping controller. In Fig. 3, the transfer function of the PM motor $G(s)$ is expressed as

$$G(s) = \frac{1}{R_a + sL_m} \quad (3).$$

The open-loop transfer function $T(s)$ is given by

$$T(s) = PI(s)G(s) = \frac{\omega_c}{s} \quad (4).$$

The open-loop transfer function is the same as the integral form.

C. The damping controller integrated into the output current control loop

Fig. 4 shows the control block diagram of each unit with the proposed damping controller integrated into the output current control loop. The damping controller $H(s)$ is inserted into the feedback path of the q-axis current control loop. The damping controller $H(s)$ is expressed as

$$H(s) = K_{damp} \frac{sT_{hpf}}{1+sT_{hpf}} \quad (5),$$

where K_{damp} is the damping gain, and T_{hpf} is the time constant of the high pass filter. In addition, the first-order delay $F(s)$ is inserted into the q-axis current command in order to cancel the zero of the damping controller and prevent a large overshoot. The first-order delay $F(s)$ is expressed as

$$F(s) = \frac{1}{1+sT_{hpf}} \quad (6).$$

The loop gain of the current controller with the damping controller $T_{damp}(s)$ is given by (7).

$$T_{damp}(s) = PI(s)G(s)\{1-H(s)\} = \frac{\omega_c}{s} \frac{sT_{hpf}(1-K_{damp})}{1+sT_{hpf}} \quad (7)$$

The transfer function of the feedback path {1-$H(s)$} is the same form as a phase delay compensator.

Fig. 5 shows the bode diagram of the current control loop gain $T(s)$ and $T_{damp}(s)$. The loop gain with the damping controller is reduced at a high-frequency range. The damping controller stabilizes the system by decreasing the loop gain.

The closed-loop transfer function of the current controller with the damping controller $G_{close}(s)$ is derived as

$$G_{close}(s) = \frac{\omega_c / T_{hpf}}{s^2 + \frac{1+T_{hpf}\omega_c(1-K_{damp})}{T_{hpf}} s + \frac{\omega_c}{T_{hpf}}} \quad (8).$$

Equation (8) is the same form as a second-order standard form. The second-order standard form is expressed as

$$G_{SOSF}(s) = \frac{\omega_n^{\ 2}}{s^2 + 2\zeta\omega_n s + \omega_n^{\ 2}} \quad (9),$$

where ζ is the damping factor, and ω_n is the natural angular frequency. The damping factor ζ and the natural angular frequency ω_n of the current controller with the damping controller are derived by comparison between (8) and (9) as

$$\zeta = \frac{1+T_{hpf}\omega_c(1-K_{damp})}{2T_{hpf}\sqrt{\omega_c / T_{hpf}}} \quad (10),$$

$$\omega_n = \sqrt{\frac{\omega_c}{T_{hpf}}} \quad (11).$$

Equation (11) means that the bandwidth of the current controller with the damping control is determined by ω_c and T_{hpf}. The system stability is improved with increasing T_{hpf} since ζ is increased, while the current response is degraded. Thus, T_{hpf} needs to be designed as small as possible in order to prevent the current response degradation.

III. Stability Analysis

The stability of the system shown in Fig. 1 is analyzed based on the impedance method, which is proposed by Middlebrook [16]. In the impedance method, the whole system is divided into source and load sides, and the system stability is determined by the Nyquist plot of the minor loop gain, which is the product of the output impedance of the source side and the input admittance of the load side.

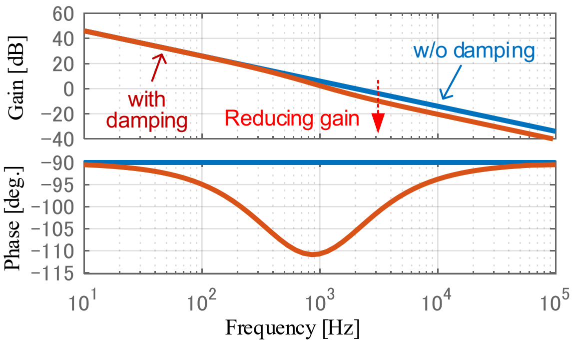

Fig. 5 The bode diagram of the current control loop gain with and without the damping controller. The damping controller reduces the loop gain at the high-frequency range.

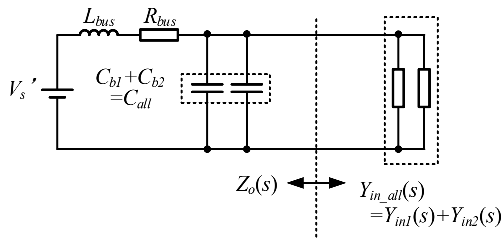

Fig. 6. The equivalent impedance model of the DC-bus servo drive system. The servo drivers are expressed as the input admittance. This model consists of the LC filter and the combined admittance.

A. The impedance of each subsystem

Fig. 6 shows the equivalent impedance model of the DC-bus servo drive system. In Fig. 6, the servo drivers and motors of each unit are expressed as the input admittance $Y_{in1}(s)$ and $Y_{in2}(s)$. The equivalent impedance model consists of the LC filter and the combined admittance $Y_{in\_all}(s)$. Here, the output impedance of the LC filter $Z_o(s)$ is expressed as

$$Z_o(s) = \frac{sL_{bus} + R_{bus}}{s^2 L_{bus}C_{bus} + sC_{bus}R_{bus} + 1} \quad (12).$$

The input admittance of each servo unit is derived by the extra element theorem [6][16]. The input admittance of a constant power load $Y_{CPL}(s)$ is expressed as

$$Y_{CPL}(s) = \frac{1}{Z_N(s)} \frac{T(s)}{1+T(s)} + \frac{1}{Z_D(s)} \frac{1}{1+T(s)} \quad (13),$$

where $Z_N(s)$ is the input impedance of the constant power load with ideal feedback, and $Z_D(s)$ is the input impedance without feedback. The input impedance of the servo driver with ideal feedback $Z_N(s)$ is expressed as

$$Z_N(s) = -\frac{V_{b,0}}{I_{b,0}} = -\frac{V_{b,0}^{\ 2}}{P_{out}} = -\frac{V_{b,0}^{\ 2}}{(I_{q,0}R_a + \omega_{re}K_e)I_{q,0}} \quad (14),$$

where $V_{b,0}$ is the steady value of the DC-link voltage, $I_{b,0}$ is the steady value of the DC-link current, P_{out} is the output power of the servo driver, and $I_{q,0}$ is the steady value of the q-axis current. Note that $Z_N(s)$ is a negative impedance depending on the motor output power.

The input impedance of the servo driver without feedback $Z_D(s)$ is expressed as

$$Z_D(s)=\frac{1}{\alpha^2}\left(R_a+sL_m\right)=\left(\frac{V_{b,0}}{R_aI_{q,0}+\omega_{re}K_w}\right)^2\left(R_a+sL_m\right) \quad (15),$$

where α is the conversion ratio from the DC-link voltage to the q-axis voltage.

The input admittance of the servo driver $Y_{in}(s)$ is derived by substituting (13)-(15) as (16).

$$Y_{in}(s)=-\frac{I_{q,0}\left(R_aI_{q,0}+\omega_{re}K_e\right)}{V_{b,0}{}^2}\frac{T(s)}{1+T(s)}+\frac{\left(R_aI_{q,0}+\omega_{re}K_e\right)^2}{V_{b,0}{}^2\left(R_a+sL_m\right)}\frac{1}{1+T(s)} \quad (16)$$

Fig. 7 shows the bode diagram of the input admittance $Y_{in}(s)$. The input admittance of the servo driver changes depending on its operation points, such as the torque (q-axis current) and the motor speed. The phase in the lower frequency range is near 180 deg when the motor outputs the torque. This means that the servo driver has negative resistance characteristics.

B. The stability analysis

The stability of the system shown in Fig. 6 is analyzed by the Nyquist plot of the minor loop gain, which is the product of the $Z_o(s)$ and $Y_{in\_all}(s)$. The minor loop gain of the system $T_{MLG}(s)$ is expressed as (17).

$$T_{NLG}(s)=Z_o(s)Y_{in\_all}(s)=Z_o(s)Y_{in1}(s)+Z_o(s)Y_{in2}(s) \quad (17)$$

The minor loop gain of the whole system is expressed as the sum of the minor loop gains of each unit. The minor loop gains of each unit are expressed as $T_{MLG1}(s)$ and $T_{MLG2}(s)$.

Fig. 8 shows the bode diagram of the minor loop gain of the whole system $T_{MLG}(s)$ and each unit $T_{MLG1}(s)$ and $T_{MLG2}(s)$. The gain and phase are changed sharply at the resonant frequency f_{res} of the LC filter. The phase crossover frequency f_o of each minor loop gain is almost the same near the resonant frequency. The minor loop gain of the whole system at the phase crossover frequency $T_{MLG}(f_o)$ is expressed under the condition that the phase crossover frequency of each unit is the same as

$$\begin{aligned}T_{MLG}(f_o)&=\mathrm{Re}\left\{T_{MLG}(f_o)\right\}\\&=\mathrm{Re}\left\{T_{MLG1}(f_o)\right\}+\mathrm{Re}\left\{T_{MLG2}(f_o)\right\}\end{aligned} \quad (18)$$

$$\because \mathrm{Im}\left\{T_{MLG}(f_o)\right\}=\mathrm{Im}\left\{T_{MLG1}(f_o)\right\}=\mathrm{Im}\left\{T_{MLG2}(f_o)\right\}=0$$

Fig. 9 shows the Nyquist plot of the minor loop gains of the whole system $T_{MLG}(s)$ and each unit $T_{MLG1}(s)$ and $T_{MLG2}(s)$. The gain margin of a system corresponds to the reciprocal of the real part of minor loop gain at the phase crossover frequency. The relationship between the gain margins and the minor loop gains is expressed as

$$\mathrm{Re}\left\{T_{MLG}(f_o)\right\}=-GM_{all} \quad (19),$$

$$\mathrm{Re}\left\{T_{MLG1}(f_o)\right\}=-GM_1 \quad (20),$$

$$\mathrm{Re}\left\{T_{MLG2}(f_o)\right\}=-GM_2 \quad (21),$$

where GM_{all} is the gain margin of the whole system in dB, and GM_1 and GM_2 are the gain margins of each unit in dB. Thus,

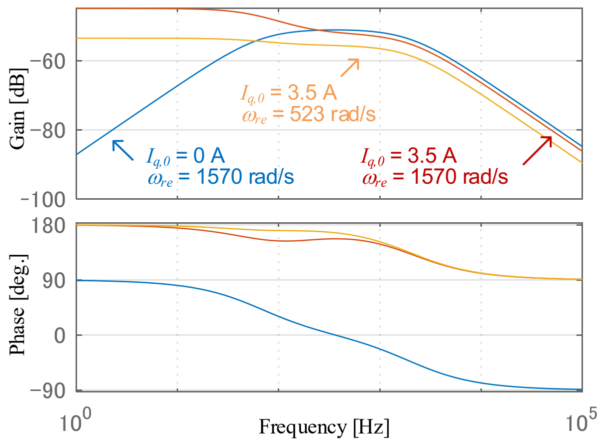

Fig. 7. The input admittance of the servo driver. The input admittance changes depending on the operation point of the servo motor.

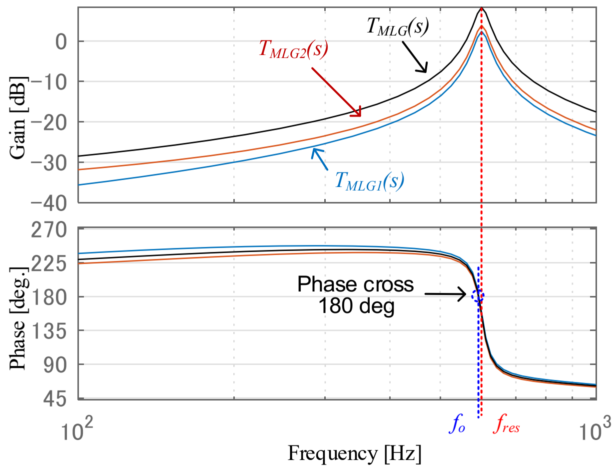

Fig. 8. The bode diagram of the minor loop gain of the whole system and each unit. The phase crossover frequency of each minor loop gain is almost the same near the resonant frequency of the LC filter.

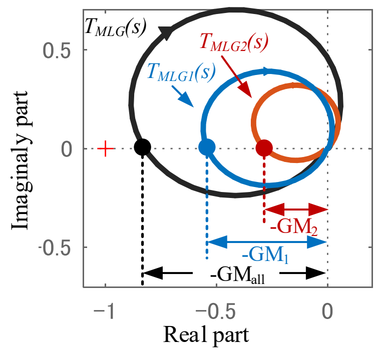

Fig. 9. The Nyquist plot of the minor loop gains of the whole system and each unit. The gain margin is the reciprocal of the real part of the minor loop gain at the phase crossover frequency.

The relationship between the gain margin of the whole system and each unit is given by (22).

$$GM_{all}=GM_1+GM_2 \quad (22)$$

As shown in (22), the gain margin of the whole system is expressed as the sum of the gain margins of each unit in the DC-bus servo drive system.

IV. Proposed Parameter Design Method

This section proposes the parameters of the damping controller design method for multiple DC-bus servo drive systems based on the relationship of the gain margins.

A. Design flow

Fig. 10 shows the proposed parameters design flow for multiple DC-bus servo drive systems. The proposed flow consists of three steps. At first, the minimum gain margin of the whole system GM_{all} is set. Second, the minimum gain margin of each unit GM_k is set based on GM_{all}. Finally, the parameters of the damping controller of each unit are tuned so that the unit ensures the desired gain margin GM_k over the all operating range of the motor. As shown in (22), the whole system ensures the minimum gain margin GM_{all} when all units ensure GM_k.

Fig. 10(b) shows the subroutine for tuning the damping parameters of each unit. At first, the time constant of HPF is set to $1/\omega_c$ because the natural angular frequency ω_n is the same as ω_c when T_{hpf} is equal to $1/\omega_c$. Second, the damping gain K_{damp} is calculated by (23), which is derived by (10).

$$K_{damp} = \frac{1+T_{hpf}\omega_c}{T_{hpf}\omega_c} - 2\zeta\sqrt{\frac{1}{T_{hpf}\omega_c}} \tag{23}$$

If the system does not satisfy GM_k, T_{hpf} is changed, and K_{damp} is calculated again. If the system satisfies GM_k, the design of the damping parameters is finished.

B. The parameters design

Table 1 shows the parameters of the system. The same two units are connected to a common DC-bus line. In this paper, the parameters are designed in order to be stable within the range of rated torque and speed. In general, the gain margin of the whole system GM_{all} is set to less than 0dB. In this paper, GM_{all} is set to 0 dB in order to check the validity of the design from the waveform. In addition, the gain margin of each unit GM_k is set to 6 dB, which is twice of GM_{all}, because the two same units are connected to the DC-bus line.

Fig. 11 shows the relationship between the motor speed and the gain margin of one unit when the q-axis current is rated current of 3.5 A. As a result of the design, the time constant T_{hpf} is set to 0.765 msec, and The damping gain K_{damp} is set to be 0.648 when ζ is 0.707. The natural angular frequency of the current controller with the damping ω_n, which is calculated by (11), is 4053 rad/s. The gain margin of the unit with the damping controller has a bottom with increasing the motor speed at 1340 r/min.

Fig. 12 shows the gain margin of the whole system calculated by (22), and the true value, which is calculated by the transfer function of the whole system based on (17). In Fig. 12, Unit #1 is driven at the operation point where the gain margin of Unit #1 is minimum, and the motor speed of Unit #2 is changed. The gain margin of calculated by (22) and the true value is agreed in the range from low speed to the speed at which the gain margin is bottom. However, the proposed analysis based on (22) underestimates the whole system's stability in the high-speed range. The error occurs because the phase crossover frequency of Unit #2 is shifted to the lower frequency side due to the influence of the positive term of the input admittance $Y_{in}(s)$.

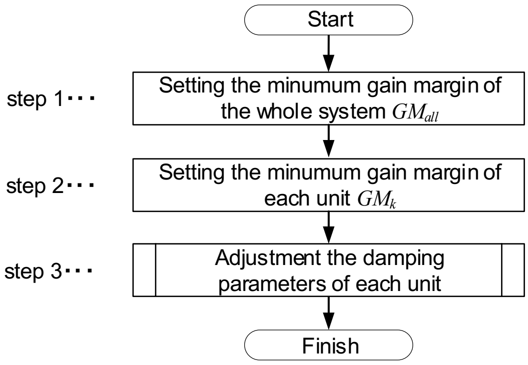

(a) The flow chart for the design of the Dc-bus servo drive system

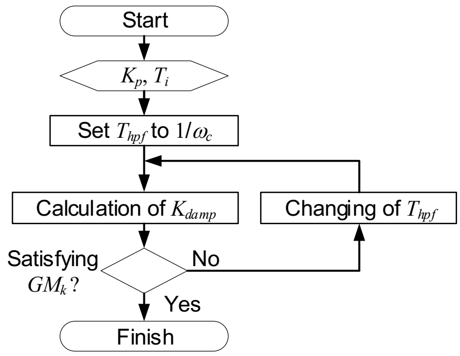

(b) The subroutine for adjustment of the damping parameter of each unit

Fig. 10. The proposed design flow for the damping controller of the DC-bus servo drive system. The gain margin of the whole system is satisfied when each unit satisfies the minimum gain margin GM_k.

Table 1 The parameters of the DC-bus servo drive system.

	Circuit	
L_{bus}	Wiring indutance of DC Bus	11 mH
R_{bus}	Wiring resistance of DC Bus	2.2 Ω
C_{b1}, C_{b2}	Inverter input capasitance	6.8 µF
V_{dc}	DC bus voltage	280 V
	Controller	
ω_c	The bandwidth of current controller	4000π rad/s
K_p	Proportional gain	42.7
T_i	Integration time	2.43 ms
f_{sw}	Switching frequency	20 kHz
f_{samp}	Sampling frequency	20 kHz
T_d	Dead time	2 µs
	Drive Side Motor (Unit #1, #2) R88M-1M40030T (Omron)	

Fig. 13 shows the bus current waveform when both units are driven at the operation point where the gain margin is minimum. Note that the simulation model includes the ideal controller, which is not considered the delays. The continuous oscillation occurs because the whole system becomes the stable limit. This result shows that the proposed design method is valid for the design of the DC-bus servo drive system.

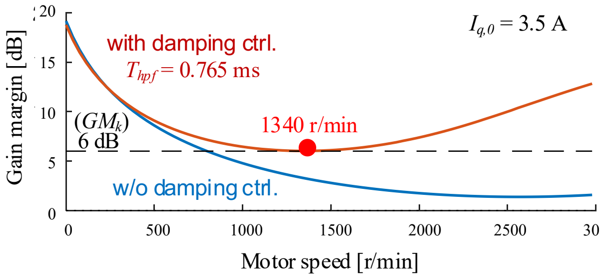

Fig. 11. The relationship between the motor speed and the gain margin of each unit. With the damping controller, the unit satisfies GMk within the rated current and speed.

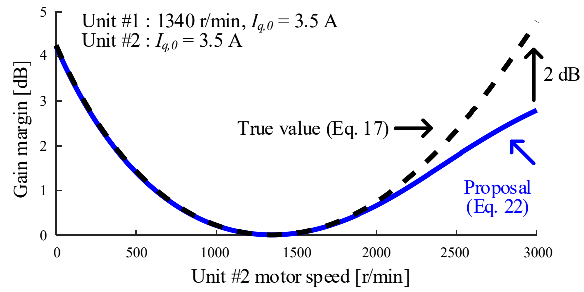

Fig. 12. The relationship between the Unit #2 motor speed and the gain margin of the whole system. The operation point of Unit #1 is constant at the point that the gain margin is minimum. The error occurs in the high-speed range because the phase crossover frequency of Unit #2 is shifted to the lower frequency.

V. Experimental Results and Discussion

This section evaluates the validity of the proposed parameters design method in the experiment. The parameters in the experiment are based on Table 1. The motor speed is controlled by the load-side motor.

A. The current response

Fig. 14 shows the step response of the q-axis current by the standard second-order form, the experimental, and the simulation. Note that the simulation model includes the controller with the PWM delay and the discretization. The overshoot in simulation and experiment is larger than that of the standard second-order form due to the influence of the PWM delay and the resonant of the LC filter. The overshoot value and the peak arrival time in the experiment agree with that of the simulation result within 1%.

B. The damping effect

Fig. 15 shows the bus current waveform with the proposed damping controller. The oscillation occurs in the period without the damping controller because the system becomes unstable. The oscillation is suppressed when the damping controller is tuned on. Thus, the proposed damping controller suppresses the oscillation of the DC-bus current effectively.

Fig. 16 shows the stable operation area when two motors are driven in the experiment, the analysis, and the simulation. Unit #1 motor is driven at 3000 r/min, and Unit #2 is driven at 1500 r/min. Note that the simulation model includes the controller with the PWM delay. The stable limit output of one unit is changed depending on another unit's output. The stable operation area in the experiment is expanded by 28% of the motor-rated power by the damping controller. However, the stable operation area in the experimental is reduced by 40% of the motor-rated power compared to the analysis. The result of the simulation is reduced error with the experimental. Thus, this result shows that the delays in the controller influence the system's stability.

C. Discussion

This section discusses the impact of the PWM delay on the system's stability. Fig. 17 shows the block diagram of each unit with the damping controller and PWM delay. The delay time of the controller with PWM is 1.5 times the sampling period.

Fig. 18 shows the input admittance of the servo unit with the damping controller with and without delay. The gain is increased near the natural frequency f_n by the PWM delay.

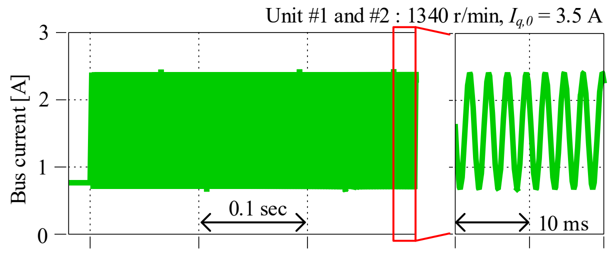

Fig. 13. The bus current waveform in the simulation. Both units are driven at the operation point where the gain margin is minimum. The continuous oscillation occurs because the whole system is a stable limit.

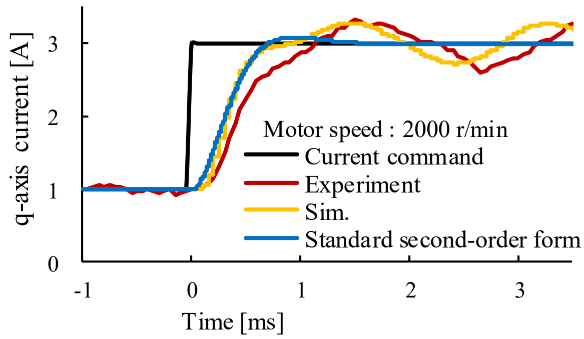

Fig. 14. The step response of the q-axis current by the standard second-order form, the experimental, and the simulation. The overshoot value and the peak arrival time in the experiment agree with that of the simulation result within 1%.

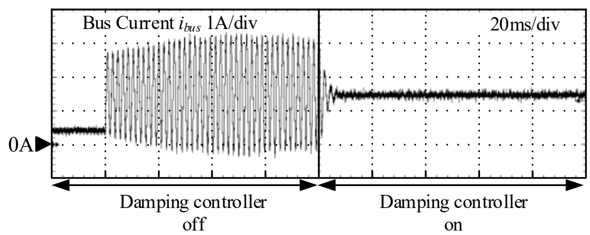

Fig. 15. The DC-bus current waveform when the damping controller is turned on. The oscillation due to the system instability is suppressed effectively.

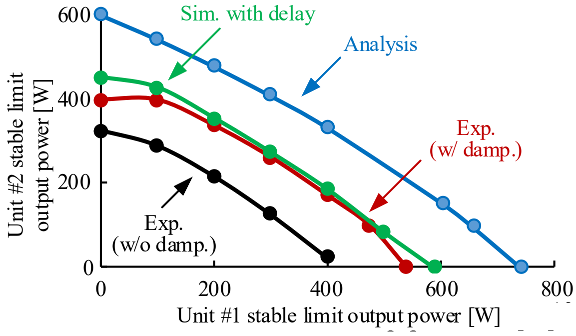

Fig. 16. The operation area when two motors are driven. Unit #1 is driven at 3000 r/min, and unit #2 is driven at 1500 r/min. The stable operation area with the damping controller is expanded by 28% of the motor-rated power.

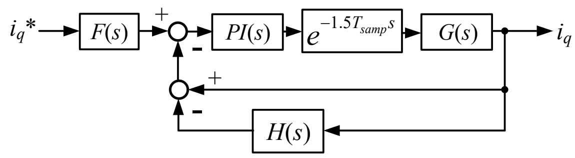

Fig. 17. The block diagram of each unit with the damping controller and PWM delay. The delay is 1.5 times the sampling period.

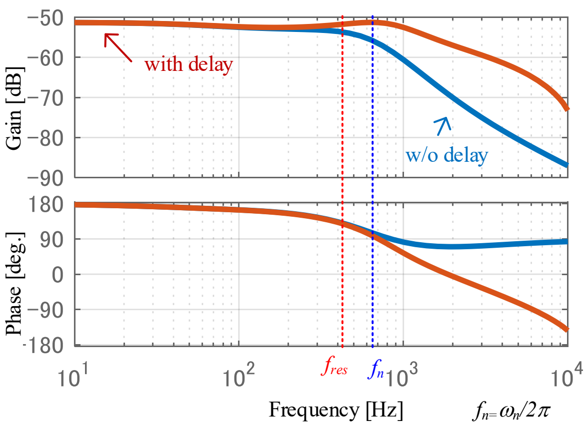

Fig. 18. The input admittance of the servo driver with the damping controller. The gain of the input admittance with the delay is increased near the natural frequency. The phase with the delay is reduced over the natural frequency.

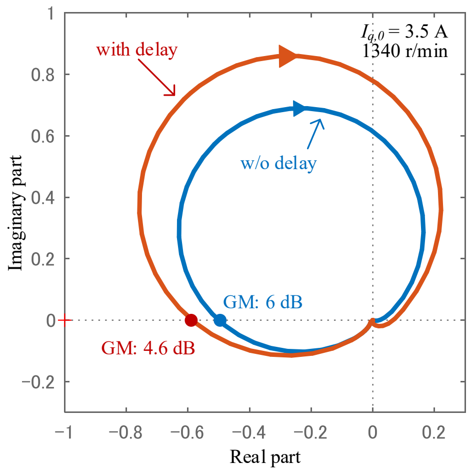

Fig. 19. The Nyquist plot of the minor loop gains of each system. The gain margin of the model with controller delay is reduced by 1.4 dB.

This factor leads to the system stability being reduced. On the other hand, the phase of the model with delay is changed from the model without the delay over the natural frequency.

Fig. 19 shows the minor loop gains of one unit with and without the PWM delay. The gain margin of the model with the delay is reduced by the model without delay with 1.4 dB because the gain of the input admittance near the resonant frequency of the LC filter is increased. As shown in Fig. 18 and 19, the delay of the controller influences the system stability when the resonant frequency of the LC filter is near or over the natural frequency. The input admittance considered the controller delay is needed to design the DC-bus servo drive system in order to consider the impact of delays.

VI. Conclusions

This paper proposed the damping control and its parameters design method for multiple servo drive units connected to a common DC-bus line. The damping controller was integrated into the q-axis current controller and evaluated the influence on the current response by compared with the second-order standard form. In addition, the parameters design method for the system with multiple units was proposed. The proposed design method was based on the impedance method and ensured the desired gain margin. The proposed method was evaluated by the analysis and the experiment. The experiment results showed that the stable operation area is expanded by 28% of the motor-rated power by the damping controller. This paper also discussed the impact of the controller delay on the system's stability.

In the future, the controller achieving both high current response and damping performance will be considered.

References

[1] N. Nakao, K. Tobari, T. Sugino, Y. Ito, M. Mishima, and D. Maeda, "Torque Ripple Suppression for PMSMs using Feedforward Compensation and Online Parameter Estimation," *IEEJ Journal of Industry Applications*, vol. 10, no. 4, pp. 497-505, 2021.

[2] M. Kakihara, M. Takaki, M. Ohto, and S. Morimoto, "Investigation of Servomotor Structure for Sensor less Control Based on High-Frequency Injection Method," *IEEJ Journal of Industry Applications*, vol. 10, no. 6, pp. 718-725, 2021.

[3] N. Kawamura, T. Zamma, K. Koiwa, K. Liu, and M. Hasegawa, "Position Sensor less Adaptive Positioning Servo System with Simplified Differential Calculation and High-Frequency Voltage Injection Strategy Considering Acoustic Noise Suppression," *IEEJ Journal of Industry Applications*, vol. 10, no. 1, pp. 1-10, 2021.

[4] T. Kai, H. Sekiguchi, and H. Ikeda, "Control Structure with Dual Acceleration Feedback for Positioning Machine with Semi-Closed Servo System," *IEEJ Journal of Industry Applications*, vol. 11, no. 2, pp. 351-358, 2022.

[5] E. Totoki, S. Yamaguchi, T. Tanaka, K. Ito, A. Daikoku, and S. Morimoto, “Torque Ripple Reduction for Permanent Magnet Motor using New Configuration for Concentrated Windings,” *IEEJ Journal of Industry Applications*, vol. 11, no. 3, pp. 531-537, 2022.

[6] T. Kiribuchi, T. Zaitsu, M. Doi, K. Kusaka, and J. Itoh, “DC-bus Systems for Servo Drives and its Stability Analysis,” in *IEEE International Conference on DC Microgrids 2019*, no. 7-A-3.

[7] A. Riccobono, and E. Santi, “Comprehensive Review of Stability Criteria for DC Power Distribution Systems,” *IEEE Transaction on Industry Applications*, vol. 50, no. 5, pp. 3525-3535, 2014.

[8] X. Feng, J. Liu, and F. D. Lee, “Impedance Specifications for Stable DC Distribution Power Systems,” *IEEE Transaction on Power Electronics*, vol. 17, no. 2, pp. 157-162, 2002.

[9] Y. Jeung, D. Lee, T. Dragicevic, and F. Blaabjerg, “Design of Passivity-Based Damping Controller for Suppressing Power Oscillations in DC Microgrids,” *IEEE Transaction on Power Electronics*, vol. 36, no. 4, pp. 4016-4028, 2021.

[10] Y. Gu, W. Li, and X. He, “Passivity-Based Control of DC Microgrid for Self-Disciplined Stabilization,” *IEEE Transaction on Power Systems*, vol. 30, no. 5, pp. 2623-2632, 2015.

[11] N. Zhao, G. Wang, R. Zhang, B. Li, Y. Bai, and D. Xu, “Inductor Current Feedback Active Damping Method for Reduced DC-Link Capacitance IPMSM Drives,” *IEEE Transaction on Power Electronics*, vol. 34, no. 5, pp. 4558-4568, 2019.

[12] J. Lee, G. Lee, S. Park, and R. Kim, “Impedance-Based Modeling and Common Bus Stability Enhancement Control Algorithm in DC Microgrid,” *IEEE Access*, vol. 8, pp. 211224-211234, 2020.

[13] X. Zhang, Q. Zhong, and W. Ming, “Stabilization of Cascaded DC/DC Converters via Adaptive Series-Virtual-Impedance Control of the Load Converter,” *IEEE Transaction on Power Electronics*, vol. 31, no. 9, pp. 6057-6063, 2016.

[14] B. He, W. Chen, X. Li, L. Shu, and X. Ruan, "A Power Adaptive Impedance Reshaping Strategy for Cascaded DC System With Buck-Type Constant Power Load," *IEEE Transaction on Power Electronics*, vol. 32, no. 8, pp. 8909-8920, 2022.

[15] M. Hassan, C. Su, F. Chen, and K. Lo, “Adaptive Passivity-Based Control of a DC-DC Boost Power Converter Supplying Constant Power and Constant Voltage Loads,” *IEEE Transaction on Industrial Electronics*, vol. 69, no. 6, pp. 6204-6214, 2021.

[16] R. D. Middlebrook, “Input Filter Considerations in Design and Application of Switching Regulators,” in *Proc. of IEEE Industrial Application Society Annual Meeting*, pp. 366-382, 1976.

[17] H. Takahashi, and J. Itoh, “Design Procedure for Output Current Control and Damping Control of Matrix Converter,” in *the 2014 International Power Electronics Conference*, no. 19P1-14, pp. 152-159.